Electronic Supplementary Information (ESI)

STEP Cement: Solar Thermal Electrochemical Production of CaO without CO_2 emission (Chemical Communications)

Stuart Licht,[*,a] Hongjun Wu,[a,b] Chaminda Hettige,[a] Baohui Wang,[a,b] Joseph Asercion,[a] Jason Lau,[a] Jessica Stuart[a]

*CORRESPONDING AUTHOR EMAIL ADDRESS: slicht@gwu.edu

[a] Department of Chemistry, George Washington University, Washington, DC 20052, USA.

[b] Present address: Northeast Petroleum University, Daqing, P. R. China

Content

Cement production accounts for 5-6% of all anthropogenic CO_2 emissions. Massive CO_2 emissions also occur with the CaO formed from $CaCO_3$ for purifying iron and aluminum, for agriculture, glass, paper, sugar, calcium carbide, and acetylene production, to scrub SO_2 from smoke stacks, to soften water or to remove phosphates from sewerage.[12,13] ClimateCentral.org recently wrote that no other sector has such a high potential for drastic emission reductions, and while other processes are being explored to sequester cement's CO_2, none eliminate it. Society consumes over $3x10^{12}$ kg of cement annually, and the cement industry releases 9 kg of CO_2 for each 10 kg of cement produced. An alternative to this CO_2 intensive process is needed. The majority of CO_2 emissions occurs during the decarbonation of limestone ($CaCO_3$) to lime (CaO) described in equation 1, and the remainder (30 to 40%) from burning fossil fuels, such as coal, to heat the kiln reactors to ~900°C, eq. 2:[1-3]

In this Chemical Communications and Electronic Supplementary Infromration, we show a new thermal chemistry, based on anomalies in oxide solubilites, to generate CaO, without CO_2 emission, in a high throughput, cost effective, environment conducive to the formation of cement.

Expanded experimental details:

Thermodynamic calculations

Electrolysis potentials are calculated from the thermochemical enthalpies and entropies of the reactants.[14,15]

Chemicals, materials, electrolysis configurations

Lithium carbonate was utilized (Li_2CO_3, Alfa Aeasar, 99%), lithium oxide (Li_2O (99.5%, Alfa Aeasar), sodium carbonate (Na_2CO_3, Avantor 99.5%), potassium carbonate (K_2CO_3, Avantor 99%), Ni foil (pure Ni 200 McMaster 9707K59), Ni wire (1 mm diameter, 99.5%, Alfa Aeasar), steel wire (14 gauge), 25 and 75 μm nickel and steel sheet (McMaster 95481, 97057), and various crucibles: nickel (Alfa Aeasar 35904), steel (VWR 82027), and high purity alumina (99.6% AdValue Technology); crucibles were encased in high temperature foam insulation (McMaster 9353).

Figure 3. Configurations and components used in the STEP electrolysis experiments. Left side: three electrolyses in series, with lithium carbonate using thin planar nickel and steel electrodes, prior to the melt, and prior to addition of external insulation. Middle: high surface area nickel electrode prepared by folding a single rectangle of pure nickel (25µm or 75µm thick), connected by spot welded nickel wire (99.5%. 1.0 mm) situated above a cathode for carbon deposition prepared by coiling steel wire, and is shown prior to insertion in the alumina crucible and prior o carbonate addition. Gas evolved from the central electrode can be directed with a large circumference alumina tube (not shown). Right side, high temperature configuration: coiled steel wire cathode in a nickel crucible, which acts both as the cell case and the anode, and is shown prior to the addition of the internal carbonate and external insulation.

Molten carbonate electrolytic synthesis operates in the reverse mode of molten carbonate fuel cells (MCFC); where rather than fuel injection with electricity as a product, electrical energy is supplied and energetic chemical products are generated. MCFC systems have been studied in greater depth than carbonate electrolysis systems. In one MCFC study, the addition of 10 mol% of $CaCO_3$ to molten carbonate (either $Li_{1.04}Na_{0.96}CO_3$ with 30 mol% $CaCO_3$, or $Li_{1.24}Na_{0.76}CO_3$ with 10 mol% $CaCO_3$) led to a decrease of 50mV in the 150 mA cm^{-2} cell potential at 600 to 700 °C.[17]

Configurations and components used in the STEP electrolysis experiments are shown in Figure 3. Effective anodes include the inner submerged walls (28cm^2) of a 20 ml straight walled nickel crucible, coiled pure nickel wire, and pure, nickel sheet. Steel in various shapes is effective as a cathode including coiled steel wire, and steel, and the inner submerged walls of a straight walled steel crucible. Electrolysis measurements at constant cathodic current density are made with a nickel crucible whose inner walls (with surface area ~60 fold larger than the anode) contact the electrolyte and serve as the anode counter electrode. The constant anodic current density measurements are made with a steel crucible whose inner walls in contact with the electrolyte serve as the cathode counter electrode. These measurements are made with an oversized counter electrode (28 cm^2 cathode for the 0.5 cm^2 anode measurements, and a 28 cm^2 anode for the 0.5 cm^2 cathode current density measurements). Unlike steel, pure nickel as a cathode exhibits a potential shift until coated with electrodeposited carbon, and therefore steel was used as a cathode. While highly stable in lithium carbonate electrolytes, nickel anodes tend to corrode into sodium and potassium carbonate, observable as a green coloration developing in the electrolyte during extended electrolyses. This corrosion decreases when calcium carbonate is in the electrolyte. In molten $CaCl_2$ it was previously found that NiO solubility decreased with up to 4 mol% CaO concentration, and Ni coated with NiO had much higher stability during anodic polarization .[12] In general the strength of an oxide in melts to donate an electron pair (Lewis basicity) decreases in the order: K_2O > Na_2O > Li_2O > BaO > CaO > MgO > Fe_2O_3 > Al_2O_3 > TiO_2 > B_2O_3 > SiO_2 > P_2O_5.[13] Ni is a useful cell or electrode candidate material in MCFCs, but slowly degrades via a soluble nickel oxide overlayer. Cassir *et al*. report the of addition of 10% $CaCO_3$ to 650 °C $Li_{1.04}Na_{0.96}CaCO_3$ is useful to decrease the solubility of NiO from 150 to 100 µmolal in the carbonate mix.[18]

We find that iridium is remarkably stable for the oxygen evolution reaction (OER) with no evidence of mass loss or oxidation after hundreds of hours of anode operation over a wide range of current densities, even at higher temperatures even as high as 950 °C in molten lithium carbonate).[9] In comparison, nickel, is less stable, but also suitable, and develops a protective oxide overlayer with the onset of anodic current, which is effective for facile charge transfer in the OER. In the calcium containing 750°C molten lithium carbonate electrolytes, thin (25 μm) sheet pure nickel (Ni 200, McMaster 97057K51) maintains structural integrity, with no visible signs of corrosion, as a high current anode. The right portion of Figure summarizes measured 1 cathode (open symbols) and anode (closed symbols) constrained electrolysis potentials. In this high carbonate activity media, at low current densities the electrolysis potentials are seen to be less than the unit activity thermodynamic values calculated on the right side of the figure. The addition of calcium carbonate increases the electrolysis potential at high current density, and as recently presented (not shown in Figure 1) the addition of lithium oxide decreases the electrolysis potential.[9]

In the anode constrained measurements portion of Figure 1 (solid symbols), it is seen that electrolysis can be sustained at very high current densities, and that in this high current density domain, the dissolution of 1.6 m calcium carbonate in the carbonate eutectic increases the electrolysis potential by ~400 mV. The electrolysis potential is similar with either a 0.5 cm^2 nickel or iridium anode, but is marginally (not shown) higher when measured with a 0.5 cm^2 platinum anode. The right side of Figure 1 also summarizes cathode constrained electrolysis potentials (open symbols) made with steel, an effective cathode for the electrolysis in either the eutectic carbonate or the lithium carbonate. At 500 or 750°C the cathode product, solid carbon, forms readily from molten carbonates, and at higher temperature the cathode product switches to carbon monoxide formation.

Among the pure alkali carbonates, Li_2CO_3 has the lowest melting point at 723°C. Mixed alkali carbonate melting points can be low, including 399°C for the $Li_{0.90}Na_{0.62}K_{0.48}CO_3$ mix used in Figure 2, and 695°C for the $Na_{1.23}K_{0.77}CO_3$ eutectic salts. $CaCO_3$, as aragonite, decomposes at 825 °C, and as calcite melts at 1339 °C.[19] A variety of molten carbonates have been characterized with, and without, added calcium carbonates.[14-15,20-23] The addition of calcium carbonate can decrease the melting point of a carbonate mix. The sodium/lithium carbonate eutectic, $Li_{1.07}Na_{0.93}CO_3$, has a melting point of 499°C, but decreases to below 450°C if 2 to 10 mol% equimolar $CaCO_3$ and $BaCO_3$ is added.[15]

Measurements of electrolyte stability (next section) and certain electrolyses are conducted in pure alumina, rather than metal crucibles. In the highest temperature (950°C) domain, the alumina crucible slowly reacts with concentrated Li_2O to form soluble lithium aluminate. In working electrolysis cells, we avoid this oxidative attack by using stainless steel cases, which are maintained under cathodic bias, and externally encased in high temperature foam insulation; nickel crucibles are also moderately stable under these conditions.

Carbonate stability

Today CaO for cement is made by the thermal decomposition of solid $CaCO_3$ at 900°C in accord with equation 1. At low temperatures, such as for a 500°C eutectic, molten carbonates are highly stable. With increasing temperature molten metal carbonates will chemically decompose, releasing carbon dioxide and forming the metal oxide, such as for lithium carbonate:

$$Li_2CO_3 \rightleftharpoons Li_2O + CO_2 \quad (5)$$

When exposed to atmospheric CO_2, carbonate electrolytes can decompose at higher temperatures. This is prevented with oxide addition, or increase in the CO_2 concentration as the equilibrium in equation 5 is shifted to the left. For example exposed to air, a 750 °C Li_2CO_3 with 5 m Li_2O readily gains mass in time. This is significant as it eliminates the need to pre-concentrate CO_2, and provides a path for the direct absorption (and STEP removal) of atmospheric carbon dioxide.[8,9]

We have previously calculated the variation of equilibrium equation 5 as a function of temperature and the available thermochemical data (*7*). The addition of either Li_2O (dissolved) or CO_2 (by replacing air, with pure CO_2 above the melt, displaces the reaction to the left and prevents decomposition of the carbonate melt (*7*). Our experimental thermogravimetric analyses of carbonates under various conditions are summarized in the Table 1. As seen in the top row, and comparable to the conventional cement process, 97.5% of the initial solid calcium carbonate decomposes via release of CO_2 after 5 hours of heating at 900°C. At 750°C this value falls to 16.0%. Lithium carbonate is molten at 750°C and loses only 1.8 mol % under the same conditions. Dissolved $CaCO_3$ decomposes at a rate intermediate to pure molten Li_2CO_3 and pure solid $CaCO_3$. 12 g (6m) of $CaCO_3$ dissolved in 20 g of Li_2CO_3 exhibits 3.2% decomposition at 750°C. As expected, lowering the temperature (to 735°C) and lowering the concentration of dissolved calcium carbonate to 5 m decreases the observed decomposition (to 3.0%). Air contains 0.03% CO_2. From this CO_2, a molten Li_2CO_3 mix with 5 m Li_2O actually gains mass in time via the back reaction of equation 5, evident as a 1.6 mol% gain in carbonate in the table. This is significant as it eliminates the need to pre-concentrate CO_2, and provides a path for the direct absorption (and STEP removal) of atmospheric carbon dioxide. The measurement is quiescent; the molten mix is exposed directly to air. The rate of direct CO_2 absorption increases with stirring or when air is bubbled into the molten mix.

Oxide addition suppresses carbon dioxide emission from molten carbonates, even those containing high concentrations of calcium carbonate, such as 6 m (12 g) $CaCO_3$ in Li_2CO_3 at 750°C in Table 1. CaO is substantially less soluble than Li_2O in molten carbonates. Conditions are probed in an electrolyte containing a slight excess of CaO to recreate calcium oxide production precipitating (beyond saturation) conditions. Compared to the negligible loss with 5 m Li_2O, and the mol loss of 3.2 % carbonate loss without oxide, the addition of 0.1 m (0.06 g) Li_2O or CaO (0.11 g), respectively decreases the mol loss to 2.3 or 2.0%. These are measured under 1 atmosphere of air. However, if the concentration of carbon dioxide is increased, or if lithium oxide concentration is increased, then equilibrium equation 5 is shifted to the left (back towards the carbonate).

Table 1. *Carbonate thermal gravimetry, mass change after heating. mil-mol = millimoles, T = temperature, t = heating time. Note, mass changes are relative, and will also depend on the surface area exposed to the air (rate of mass change will decrease with decreasing surface area).*

Carbonate mil-mol	Mass, g						T °C	t h	Phase	Mass change, g, after heating	CO_2 milli-moles	Δmole carbon-ate after heating
	$CaCO_3$	Li_2CO_3	Na_2CO_3	K_2CO_3	CaO	Li_2O						mole %
200	20.003	0	0	0	0	0	900	5	solid	-8.58	-195.	-97.5%
200	20.003	0	0	0	0	0	750	5	solid	-1.40	-31.9	-16.0%
271	0	20.007	0	0	0	0	750	5	molten	-0.21	-4.79	-1.8%
391	12.001	20.001	0	0	0	0	750	5	molten	-0.56	-12.7	-3.2%
371	10.002	20.000	0	0	0	0	735	5	molten	-0.48	-11.0	-3.0%
200	0	20.003	0	0	0	3.044	750	2	molten	+0.14	+3.26	+1.6%
391	12.001	20.003			0	3.030	750	2	molten	-0.020	-0.44	-0.11%
391	12.000	20.002			0	0.061	750	5	molten	-0.40	-9.07	-2.3%
391	12.000	20.002			0.113	0	750	5	molten	-0.35	-7.85	-2.0%
253	6.932	0	9.439	13.126	0	0	750	5	molten	-0.11	-2.56	-1.0%
252	6.905	0	9.403	13.076	0	0	850	5	molten	-0.47	-10.6	-4.2%

In the presence of $CaCO_3$, molten Li_2CO_3 electrolysis forms low solubility CaO. In the absence of this limestone, Li_2CO_3 electrolysis forms highly soluble Li_2O. This electrolysis occurs at lower potential (Fig. 1 right), and prevents carbonate decomposition:

$$Li_2CO_3 \rightarrow Li_2O + C + O_2 \ (T \leq 750°C); \ Li_2CO_{3molten} \rightarrow Li_2O + CO + 1/2O_2 \ (T \sim 900°C) \quad (6)$$

At higher temperature, electrolyte decomposition is prevented during the electrolysis of calcium carbonate by electrolysis under CO_2, or by the addition of Li_2O. In the latter case, CaO will be formed when $CaCO_3$ is added at a rate to maintain a steady state concentration of Li_2O. Above, the low, saturation concentration, CaO precipitates when this limestone is added:

$$(1+x)Li_2O + xCaCO_3 \rightarrow Li_2O + xCaO \quad (7)$$

Solubility analyses and calcium oxide product analyses

Solubility is determined from multiple measurements including compositions, both approaching saturation, and also in compositions containing excess salts. Solubility was determined redundantly by (i) visible observation, (ii) calcium atomic absorption analysis, (iii) fourier transform infrared (FTIR with a Perkin Elmer Spectrum 100) and (iv) X-ray powder diffraction analysis (XRD powder diffraction data were collected on a Rigaku Miniflex diffractometer and analyzed with the Jade software package.[24] Elemental analysis was measured with an AAnalyst 100 Atomic Absorption Spectrometer from Perkin Elmer with a 4 standard point calibration curve being performed at 1ug/mL, 4 ug/mL, 8 ug/mL and 16ug/mL with a J.T. Baker 1000 ug/mL Calcium Standard in 5% Nitric Acid. The measurements, to determine calcium in the electrolyte and products, were performed in 0.540 M HCl with 0.02% Lanthanum Chloride added. As with, XRD, FTIR was determined from a sample of molten electrolyte cooled to room temperature, and compared to spectra we measure of the pure salts. FTIR is measured as a pressed pellet formed by solid mix of the sample with KBR with a fixed mass percentage of barium sulfate. In a methodology we have previously developed, the barium sulfate provides an internal non-reactive standard to quantify other salt concentrations in the sample.[25]

When oxide is formed by electrolysis in a calcium-free, lithium containing carbonate electrolyte, the oxide is soluble and disperses away from the cathode to the bulk electrolyte. When a concentration of calcium carbonate is then added to the electrolyte which is less than that of the dissolved lithium oxide in the molten carbonate, this calcium carbonate is converted to calcium oxide which precipitates from the bulk electrolyte. The calcium oxide naturally precipitates downward, as represented in Scheme 1, as it is denser than the carbonate electrolyte. The room temperature density of CaO (3.35 g/cm^3) is greater that of Li_2CO_3 (2.11 g/cm^3), Na_2CO_3 (2.54 g/cm^3), K_2CO_3 (2.29 g/cm^3), or $CaCO_3$ (2.81 (aragonite) or 2.71(calcite) g/cm^3). However, when oxide is formed by electrolysis in a calcium-containing carbonate electrolyte, the oxide is less soluble and tends to form on the cathode, where at low temperature it will be mixed with the solid carbon product. Starting with lithium oxide in the carbonate electrolyte, and sequentially adding calcium carbonate at the rate at which oxide is formed during the electrolysis, insures bulk, rather than cathode, precipitation of CaO. The calcium oxide product is more readily extracted when it precipitates downward from the bulk electrolyte, rather than when it forms at the cathode.

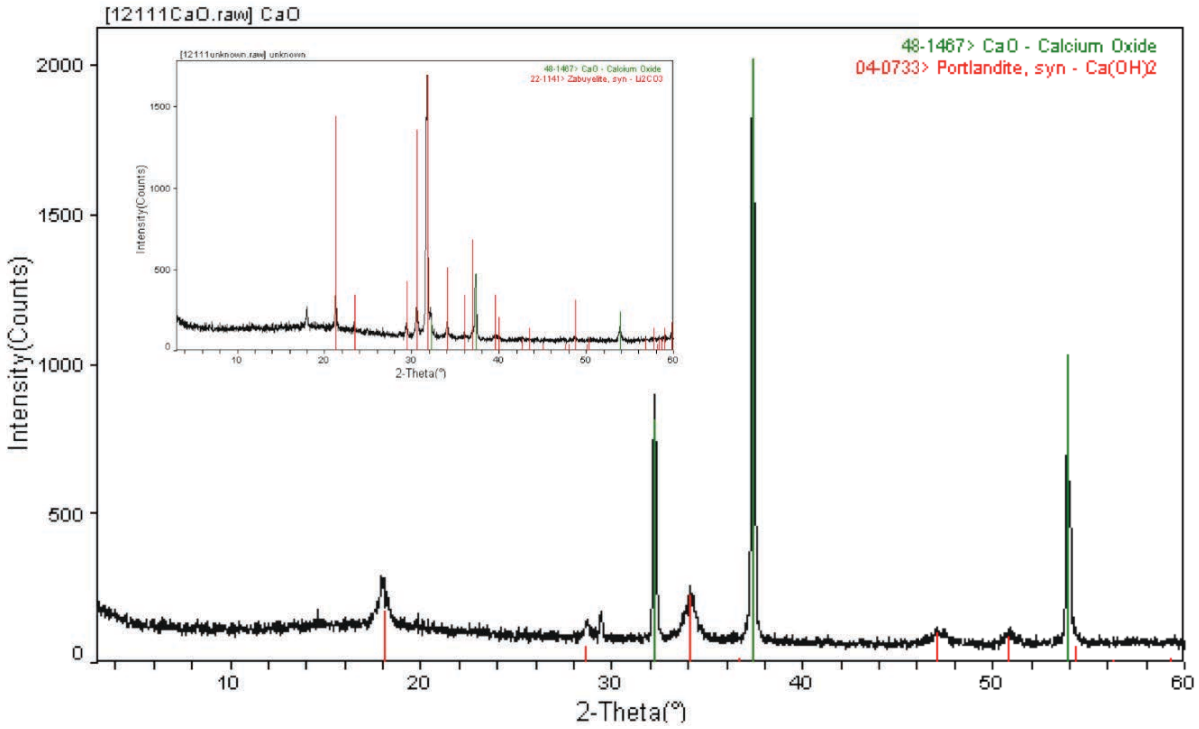

Figure 4. XRD of CaO during bulk electrolytsis of carbonate. Inset: CaO STEP product removed nearer to the electrolyte interface additionally carries clean electrolyte (Li_2CO_3), following a 5 hour 1 A electrolysis in 750°C Li_2CO_3. Library reference spectra for CaO, $Ca(OH)_2$ and Li_2CO_3 are indicated as vertical lines.

As shown by XRD in Figure 4, the CaO precipitating from the bulk electrolyte is highly pure, with some evidences of a small $Ca(OH)_2$ formation due to air exposure. CaO product removed closer to the molten carbonate interface additionally carries clean electrolyte, Li_2CO_3 as evidenced by XRD in the figure inset. The cathode is steel wire, which has been coiled into a spiral disk. After electrolysis, when the cathode wire is uncoiled at room temperature the carbon product readily drops off the wire for analysis; the steel wire used as the cathode does not exhibit any corrosion. When molten carbonate with dissolved limestone (Li_2CO_3 with $CaCO_3$) is electrolyzed instead without excess dissolved lithium oxide, the calcium oxide is tends to form near the oxide generating cathode, rather than in the bulk, and for example, can be removed along with the deposited carbon.

Analysis of coprecipated (along with reduced carbon) calcium oxide at the cathode electrolysis is a greater challenge than when calcium oxide is formed in the bulk electrolyte. Even this more challenging analysis is readily accomplished with FTIR. As shown in the upper photograph in the middle of Figure 2, the sample, containing both calcium oxide and solid carbon, is removed as a deposit on the cathode wire along with some frozen electrolyte (in this case lithium carbonate). The sample is removed by uncoiling the wire and analyzed as a pressed KBr pellet. Carbon induces a simple broad general absorption corrected from the FTIR by baseline subtraction. As shown in Figure 5, the resultant FTIR exhibits the strong absorption of CaO. At longer and shorter wavelengths, the broader spectra exhibits the distinctive Li_2CO_3 absorption in the 3645 and 1400 cm^{-1} windows due to the solidified electrolyte, and no absorption in the Li_2O absorption window of 2900 or 3700 cm^{-1}, nor the strong $CaCO_3$ absorption in the vicinity of 1800 cm^{-1}.

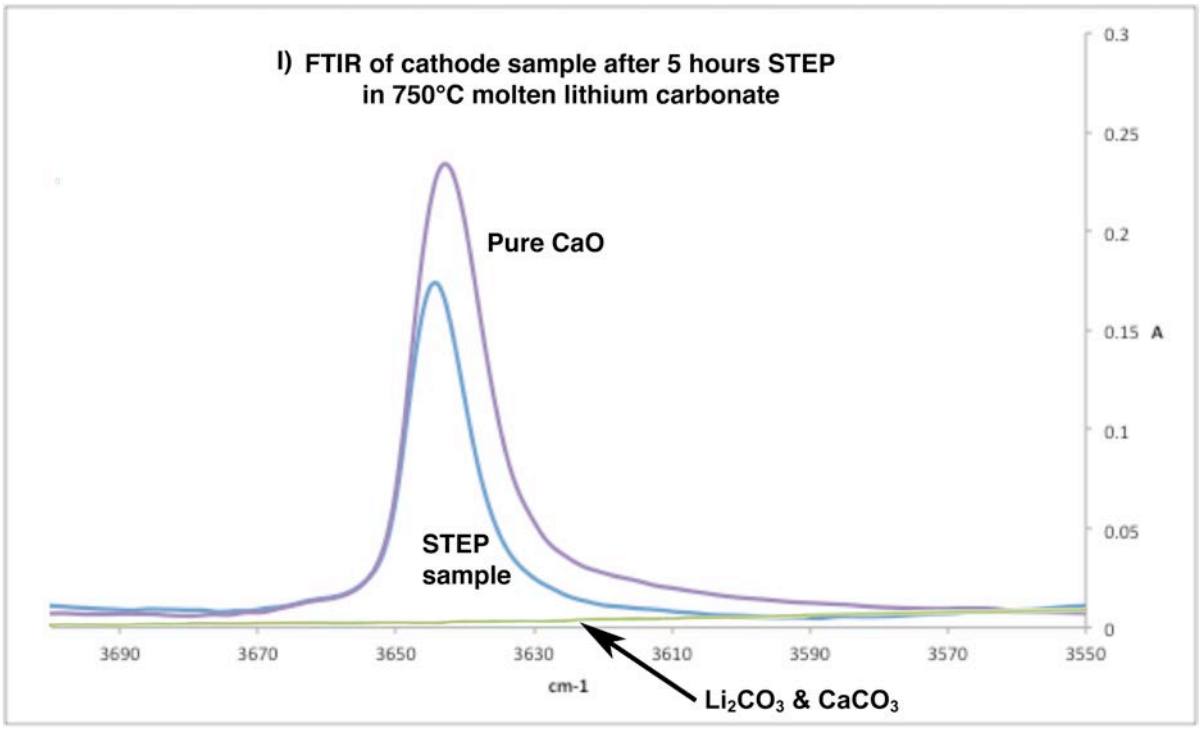

Figure 5. STEP CaO FTIR absorption spectrum of cathode deposited sample following a 5 hour 1 A electrolysis in 750°C Li_2CO_3, and following base line correction to remove broad band carbon absorption.

Economic assessment

Cement production accounts for 5-6% of all anthropogenic carbon dioxide emissions. Society consumes over 3 $x10^{12}$ kg of cement annually, and the cement industry releases ~9 kg of CO_2 for each 10 kg of cement produced. An alternative to this CO_2 intensive process is needed. The majority of the CO_2 emissions occurs during the decarbonation of calcium carbonate, $CaCO_3$, to lime, CaO, ~60% from equation 1 and the remainder from burning fossil fuels, such as coal, to heat the kiln reactors to about 900°C, eq. 2.[4,26] As with cement production, massive CO_2 emissions are associated with the CaO formed from $CaCO_3$ for purifying iron and aluminum, for agriculture, glass, paper, sugar, calcium carbide, and acetylene production, to scrub SO_2 from smoke stacks, to soften water or to remove phosphates from sewerage.[27,28]

STEP cement, in addition to forming lime without any emission of carbon dioxide, cogenerates a more valuable product than cement. The solar thermal electrolytically cogenerated product, such as CO, is produced at below current market values, and is in addition to the CaO and O_2 products. The low cost of the cogenerated product is due to the endothermic, reactive nature of the available hot carbonate from the limestone, which as demonstrated in this study, is easily reduced at high activity/low energy in the molten state to carbon or carbon monoxide. CO is an energetic industrial reagent used to produce fuels, purify nickel, and to form plastics and other hydrocarbons.

In the STEP cement process, solar thermal energy is used both for the enthalpy of calcium oxide formation from calcium carbonate and to decrease the required electrolysis potential. STEP cement can produce lime at less cost than that of conventional industry cement processes. Approximately 50% of the existing cost of the conventional carbothermal production of lime, that is $35 per ton, is for energy and $35 for materials production cost other than energy.[4,16] The projected cost of the produced calcium oxide is decreased by the value of the byproduct, either solid carbon or CO. For this analysis we explore the low voltage case (0.9 V), which generates the CO product. CO is an energetic industrial reagent used to produce fuels, purify nickel, and to form plastics and other hydrocarbons. Prices for CO are ~$600 per ton and vary with purity.[29] The CO price is intermediate to

the current value of solid carbon as either coal ($130 per ton) or graphite ($2000 per ton). The principal electrolyte Li_2CO_3 is not consumed in the production process, and is readily available (see below). Sodium and potassium carbonates are less expensive alternatives, but require further optimization for STEP cement..

Both STEP and Hy-STEP represent new solar energy conversion processes to produce energetic molecules. Individual components used in the process are rapidly maturing technologies including wind electric, (Barbier 2010) molten carbonate fuel cells (Sunmacher 2007), and solar thermal technologies (BrightSource 2012, AREVA 2012, Siemens 2011, Solar Reserve 2012, Amonix 2012, Energy Innovations 2012, Pitz-Paul 2007).

A large scale concentrator solar power (CSP) plant, including the molten salts for heat storage, is in commercial opearation,[39] albeit for electrical, rather than chemical, production, and others are following,[40] with a generated electricity cost expected to decrease from its 2010 cost of value of $0.12 to $0.09 kWh^{-1} by 2014, and equal to $2.5x10^{-5}$ per kJoule.[41] This latter value is the global, cost of CSP generated electrical power including infrastructure, costs of the solar concentration, heat storage and electrical generation. This value decreases to an upper limit of $1.2x10^{-5}$ per kJ when the heat energy is intercepted and used prior to the Carnot and friction losses of over 50% which occur in the conventional mechanical turbine of a CSP plant.

For ease of economic assessment an indirect STEP cement configuration is considered in which the same global process is simplified into known and new components. In this alternative configuration, as illustrated in the bottom portion of Scheme 1, concentrated solar thermal heats solid calcium carbonate to over 900°C producing calcium oxide and releasing hot carbon dioxide at T~900°C. As in conventional limestone to lime production, solid $CaCO_3$ is heated, albeit by solar thermal rather than fossil fuels, and the CaO is extracted as the solid emits hot CO_2. However in this indirect STEP mode, rather than being released, the hot CO_2 is electrolyzed in molten carbonate to oxygen and a carbon reduction product. The electrolyte is unchanged in the course of the electrolysis, and forms a useful, and/or storable carbon product (solid carbon at lower temperatures, or carbon monoxide at higher temperatures).

$$CaCO_{3\ solid} + Q_{solar} \rightarrow CaO_{\ solid} + CO_{2\ gas\text{-}hot} \quad (8)$$

$$\text{Low/high temp electrolysis in molten carbonate: } CO_{2\ gas\text{-}hot} \rightarrow (C + O_2) \text{ or } (CO + 1/2O_2) \quad (9)$$

Combined, eqs. 8 and 9 yield the same CO_2-free CaO production as eqs. 3 & 4. The carbonate reduction product, C or CO, is controlled by the composition and temperature of the molten carbonate.

The enthalpy required to produce CaO in equation 8, as calculated by the enthalpy of the individual components is 179 kJ/mole. For the C or CO products, the enthalpy to carbon dioxide splitting, equation 9, is respectively 394 or 283 kJ/mole. The latter is equivalent to 1.47 V, which is the thermoneutral potential. Hence for example, when CO_2 is split to CO by STEP electrolysis at 0.9 V and at 52% solar efficiency as previously described,[8] an additional 0.57 V = 108 kJ/mole of heat will sustain the process at constant temperature. In this case, the STEP reaction of one mole of $CaCO_3$ requires 287 (179 + 108) kJ/mole of thermal energy and = 0.0482 kWh (converting 2 Faraday x 0.9V) of electrical energy to cogenerate one mole of CaO and CO (as well as 0.5 moles O_2).

$$\text{STEP CaO formation with CO at 0.9V electrolysis: } CaCO_{3\ solid} + Q_{solar} + E_{renewable} \rightarrow CaO_{\ solid} + CO + 1/2O_2$$

Energy required/mole: 287 kJ of thermal energy & 0.0482 kWh of electrical energy (10)

From equation 10, the enthalpy required to drive the formation of 1 ton of CaO (17,832 moles) and 0.50 ton (17,832 moles) of CO, at 0.9V by either the indirect or direct STEP cement process in Scheme 1 is or $5.1x10^6$ kJ heat and 860 kWh of electricity. The simultaneous production cost of forming both one ton of CaO and 0.50 ton of CO is the existing $35 for materials production of lime from limestone, plus the solar thermal heat cost ($5.1x10^6$ kJ heat x $1.2x10^{-5}$ per kJ heat = $61) plus the electricity cost (860 kWh x$0.09 kWh^{-1}= $77) for a CO production cost of $173 per ton of CaO produce. The total cost per ton cost of CaO with STEP cement, is decreased by the value added of the CO byproduct.

CO value generated = CO production cost – CO market value
= \$173 per ton of CaO – 0.50 ton CO x \$600 ton^{-1} CO
= -\$127 ton^{-1} CaO

This negative cost (-\$127 ton^{-1} CaO) indicates CaO is formed as a free byproduct to the CO product, and the CO is produced at a cost below current market value. This terse analysis is not comprehensive, but is provided as a strong indicator of the cost benefit of STEP cement (even without factoring in the elimination of the carbon dioxide emission). A lower temperature STEP process (<800°C) produces graphite, which is also a valued added product. This will also decrease the cost of STEP cement, and unlike the higher temperature CO product, can be stored without container as a dense (2.25g/cm^3) solid. This terse analysis utilizes the assumption that the electrolysis unit will have a comparable cost to the conventional steam turbine electrical generator and energy distribution system that it replaces in a CSP with molten storage system, and has not included the additional considerable, societal value that the CaO is generated without CO_2 emission. The coupling of molten salt storage will permit a 24/7 operation that is independent of fluctuations in sunlight or day/night conditions. Related heat, as well as optical, coupling losses will increase system costs, while efficiency improvements, such as textured, higher surface area electrodes to decrease electrolysis voltage will decrease system costs. As previously noted, this STEP technology is applicable also to carbon dioxide utilization (carbon dioxide capture).

In summary, STEP cement is based on an unusual technology and new solubility chemistry, is cost effective and is free of CO_2 emissions, with CO or graphite cogenerated at below market cost. A related resource question is whether there is sufficient lithium carbonate, as an electrolyte of choice for the STEP carbon capture process, to produce the global CaO society consumes. Lithium carbonate availability as a global resource has been under recent scrutiny to meet the growing lithium battery market. Lithium carbonate is used, but not consumed in the STEP process (it is not a reoccurring cost). $5x10^{13}$ moles of CaO annually will require 10^{14} Faraday (mole) via STEP cement, or $3x10^{11}$ A per year. This requires 0.1 million metric tonnes of lithium carbonate, as calculated from a 2 kg/l density of lithium carbonate, and assuming that improved, rather than flat, morphology electrodes will operate at 3 A/cm^2 in an 0.5 cm thick cell. Thicker, or lower current density, cells will require proportionally more lithium carbonate. These values are viable within the current production of lithium carbonate. It has been estimated that the current global annual production of 0.13 million tons of LCE (lithium carbonate equivalents) will increase to 0.24 million tons by 2015.[42] Sodium or potassium carbonates are even more available, but will require further study as STEP cement electrolytes.

Addendum, copied with permission from: S. Licht. *Adv. Mat.* 2011, 47, 5592.

STEP theoretical background

Light driven water splitting was originally demonstrated with TiO_2 (a seminconductor with a bandgap, E_g > 3.0 eV).[43] However, only a small fraction of sunlight has sufficient energy to drive TiO_2 photoexcitation. Studies had sought to tune (lower) the semiconductor bandgap to provide a better match to the electrolysis potential.[44] In 2000, we used external multiple bandgap **PV**s (photovoltaics) to generate H_2 by splitting water at 18% solar energy conversion efficiency.[45,46] However, that room temperature process does not take advantage of additional, available thermal energy.

An alternative to tuning a seminconductor bandgap to provide a better match to the solar spectrum, is an approach to tune (lower) the electrolysis potential.[47,48] In 2002 we introduced a photo electrochemical thermal water splitting theory,[49] which was verified by experiment in 2003, for H_2 generation at over 30% solar energy conversion efficiency, and providing the first experimental demonstration that a semiconductor, such as Si (E_g = 1.1eV), with bandgap lower than the standard water splitting potential ($E°_{H2O}$(25°C) =1.23 V), can directly drive hydrogen formation.[47] With increasing temperature, the quantitative decrease in the electrochemical potential to split water to hydrogen and oxygen had been well known by the 1950's.[50,51] As early as 1980 it was noted that thermal energy could decrease the necessary energy for the generation of H_2 by electrolysis.[52] However, the process combines elements of solid state physics, insolation and electrochemical theory, complicating rigorous theoretical support of the process. Our photo electrochemical thermal water splitting model for solar/H_2 by this

process, was the first derivation of bandgap restricted, thermal enhanced, high solar water splitting efficiencies.[53] The model, predicting solar energy conversion efficiencies that exceed those of conventional photovoltaics was initially derived for AM (Air Mass) 1.5, terrestrial insolation, and later expanded to include sunlight above the atmosphere (AM0 insolation).[54] The experimental accomplishment followed, and established that the water splitting potential can be specifically tuned to match efficient photo-absorbers,[48] eliminating the challenge of tuning (varying) the semiconductor bandgap, and which can lead to over 30% solar to chemical energy conversion efficiencies. Our early process was specific to H_2 and did not incorporate the additional temperature enhancement of excess super-band gap energy and concentration enhancement of excess reactant to further decrease the electrolysis potential, in our contemporary **STEP** process.

A single, small band gap junction, such as in a silicon PV, cannot generate the minimum photopotential required to drive many room temperature electrolysis reactions, as shown in the left of Scheme 2. The advancement of such studies had focused on tuning semiconductor bandgaps[44] to provide a better match to the electrochemical potential (specifically, the water splitting potential), or by utilizing more complex, multiple bandgap structures using multiple photon excitation.[45,46] Either of these structures are not capable of excitation beyond the bandedge and can not make use of longer wavelength sunlight. Photovoltaics are limited to super-bandgap sunlight, $h\nu > E_g$, precluding use of long wavelength radiation, $h\nu < E_g$. STEP instead directs this IR sunlight to heat electrochemical reactions, and uses visible sunlight to generate electronic charge to drive these electrolyses.

Rather than tuning the bandgap to provide a better energetic match to the electrolysis potential, the **STEP** process instead tunes the redox potential to match the bandgap. The right side of Scheme 2 presents the energy diagram of a STEP process. The high temperature pathway decreases the free energy requirements for processes whose electrolysis potential decreases with increasing temperature. STEP uses solar energy to drive, otherwise energetically forbidden, pathways of charge transfer. The process combines elements of solid state physics, insolation (solar illumination) and high temperature electrochemical energy conversion. Kinetics improve, and endothermic thermodynamic potentials, decrease with increasing temperature. The result is a synergy, making use of the full spectrum of sunlight, and capturing more solar energy. **STEP** is intrinsically more efficient than other solar energy conversion processes, as it utilizes not only the visible sunlight used to drive PVs, but also utilizes the previously detrimental (due to PV thermal degradation) thermal component of sunlight, for the electrolytic formation of chemicals.

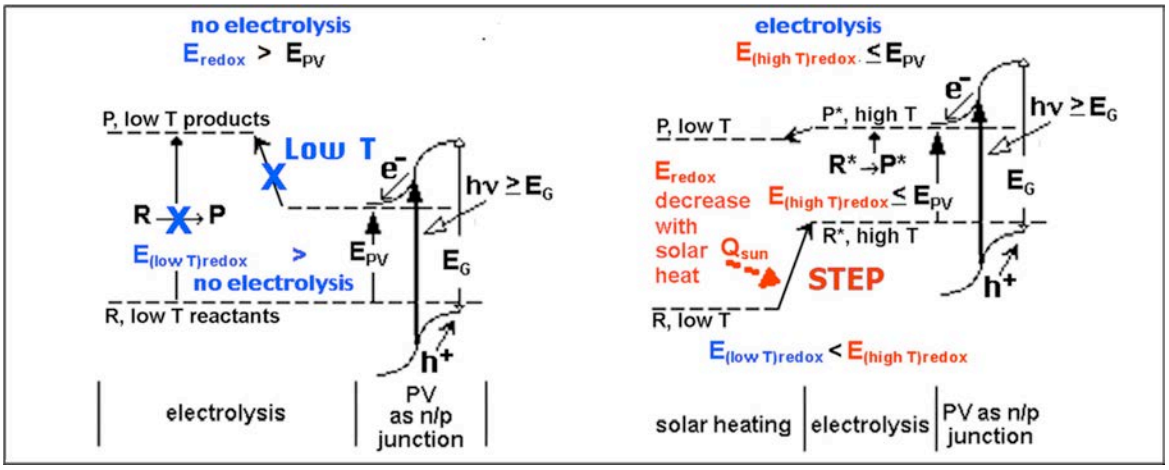

Scheme 2. Top: Comparison of PV and **STEP** solar driven electrolysis energy diagrams. STEP uses sunlight to drive otherwise energetically forbidden pathways of charge transfer. The energy of photodriven charge transfer is insufficient (left) to drive (unheated) electrolysis, but is sufficient (right) to drive endothermic electrolysis in the solar heated synergestic process. The process uses both visible & thermal solar energy for higher efficiency; thermal energy decreases the electrolysis potential forming an energetically allowed pathway to drive electrochemical charge transfer.

The two bases for improved efficiencies using the STEP process are (i) excess heat, such as unused heat in solar cells, can be used to increase the temperature of an electrolysis cell, such as for electrolytic CO_2 splitting, while (ii) the product to reactant ratio can be increased to favor the kintetic and energetic formation of reactants. With increasing temperature, the quantitative decrease in the electrochemical potential to drive a variety of electrochemical syntheses is well known, substantially decreasing the electronic energy (the electrolysis potential) required to form energetic products. The extent of the decrease in the electrolysis potential, $E_{redox,}$ may be tuned by choosing the constituents and temperature of the electrolysis. The process distinguishes radiation that is intrinsically energy sufficient to drive **PV** charge transfer, and applies all excess solar thermal energy to heat the electrolysis reaction chamber.

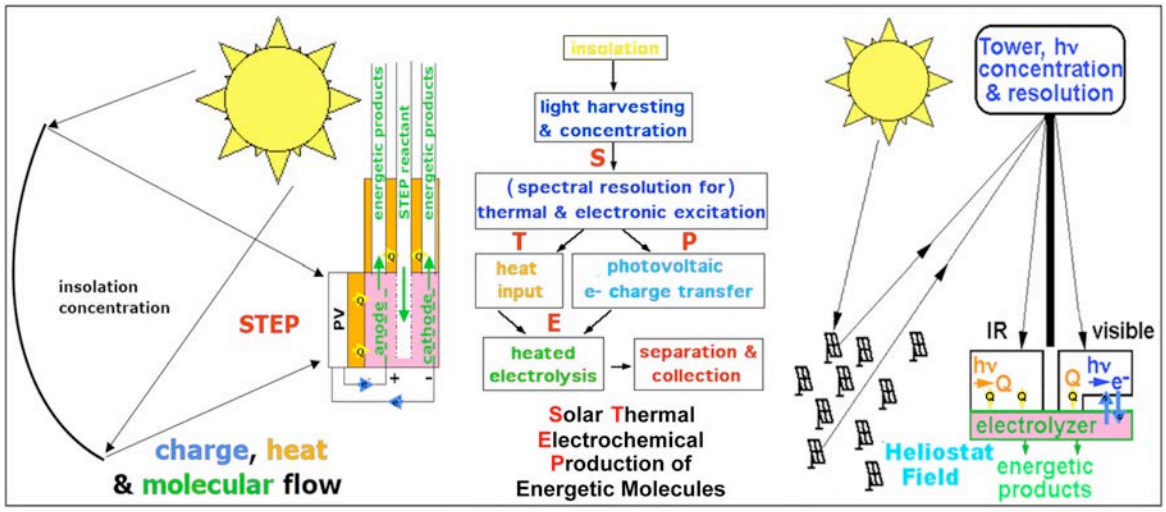

Scheme 3. Global use of sunlight to drive the formation of energy rich molecules. **Left**: Charge, & heat flow in **STEP**: heat flow (yellow arrows), electron flow (blue), & reagent flow (green). **Right**: Beam splitters redirect sub-bandgap sunlight away from the **PV** onto the electrolyzer.

Scheme 3 summarizes the charge, heat and molecular flow for the **STEP** process; the high temperature pathway decreases the potential required to drive endothermic electrolyses, and also facilitates the kinetics of charge transfer (i.e., decreases overpotential losses), which arise during electrolysis. This process consists of (i) sunlight harvesting and concentration, (ii) photovoltaic charge transfer driven by super-bandgap energy, (iii) transfer of sub-bandgap and excess super-bandgap radiation to heat the electrolysis chamber, (iv) high temperature, low energy electrolysis forming energy rich products, and (v) cycle completion by pre-heating of the electrolysis reactant through heat exchange with the energetic electrolysis products. As indicated on the right side of Scheme 3, the light harvesting can use various optical configurations; e.g. in lieu of parabolic, or Fresnel, concentrators, a heliostat/solar tower with secondary optics can achieve higher process temperatures (>1000 °C) with concentrations of ~2000 suns. Beam splitters can redirect sub-bandgap radiation away from the PV (minimzing PV heating) for a direct heat exchange with the electrolyzer.

Solar heating can decrease the energy to drive a range of electrolyses. Such processes can be determined using available entropy, S, and enthalpy, H, and free-energy, G, data,[10,11,51] and are identified by their negative isothermal temperature coefficient of the cell potential.[52] This coefficient $(dE/dT)_{isoth}$ is the derivative of the electromotive force of the isothermal cell:

$$(dE/dT)_{isoth} = \Delta S/nF = (\Delta H - \Delta G) / nFT \quad (11)$$

The starting process of modeling any STEP process is the conventional expression of a generalized electrochemical process, in a cell which drives an n electron charge transfer electrolysis reaction, comprising "x" reactants, R_i, with stoichiometric coefficients r_i, and yielding "y" products, C_i, with stoichiometric coefficients c_i.

Electrode 1 │ Electrolyte │ Electrode 2

Using the convention of $E = E_{cathode}-E_{anode}$ to describe the positive potential necessary to drive a non-spontaneous process, by transfer of n electrons in the electrolysis reaction:

n electron transfer electrolysis reaction: $\sum_{i=1 \text{ to } x} r_i R_i \rightarrow \sum_{i=1 \text{ to } y} c_i C_i$ (12)

At any electrolysis temperature, T_{STEP}, and at unit activity, the reaction has electrochemical potential, $E°_T$. This may be calculated from consistent, compiled unit activity thermochemical data sets, such as the NIST condensed phase and fluid properties data sets,[10,11] as:

$E°_T = -\Delta G°(T=T_{STEP})/nF$; $E°_{ambient} \equiv E°_T(T_{ambient})$; here $T_{ambient} = 298.15K = 25°C$,

and: $\Delta G°(T=T_{STEP}) = \sum_{i=1 \text{ to } y} c_i(H°(C_i,T)-TS°(C_i,T)) - \sum_{i=1 \text{ to } x} r_i(H°(R_i,T)-TS°(R_i,T))$ (13)

Compiled thermochemical data are often based on different reference states, while a consistent reference state is needed to understand electrolysis limiting processes, including water.[55,56] This challenge is overcome by modification of the unit activity (a=1) consistent calculated electrolysis potential to determine the potential at other reagent and product relative activities via the Nernst equation.[57,58] Electrolysis provides control of the relative amounts of reactant and generated product in a system. A substantial activity differential can also drive **STEP** improvement at elevated temperature, and will be derived. The potential variation with activity, a, of the reaction: $\sum_{i=1 \text{ to } x} r_i R_i \rightarrow \sum_{i=1 \text{ to } y} c_i C_i$, is given by:

$E_{T,a} = E°_T - (RT/nF)\cdot\ln(\prod_{i=1 \text{ to } x} a(R_i)^{r_i} / \prod_{i=1 \text{ to } y} a(C_i)^{c_i})$ (14)

Electrolysis systems with a negative isothermal temperature coefficient tend to cool as the electrolysis products are generated. Specifically in endothermic electrolytic processes, the eq 14 free-energy electrolysis potential, E_T, is less than the enthalpy based potential. This latter value is the potential at which the system temperature would remain constant during electrolysis. This thermoneutral potential, E_{tn}, is given by:

$E_{tn}(T_{STEP}) = -\Delta H(T)/nF$; $\Delta H(T_{STEP}) = \sum_{i=1 \text{ to } b} c_i H(C_i,T_{STEP}) - \sum_{i=1 \text{ to } a} r_i H(R_i,T_{STEP})$ (15)

Two general STEP implementations are being explored. Both can provide the thermoneutral energy to sustain a variety of electrolyses. The thermoneutral potential, determined from the enthalpy of a reaction, describes the energy required to sustain an electrochemical process without cooling. For example, the thermoneutral potential we have calculated and reported for CO_2 splitting to CO and O_2 at unit activities, from eq 15, is 1.46($\pm$0.01) V over the temperature range of 25-1400°C. As represented in Scheme 4 on the left, the standard electrolysis potential at room temperature, E°, can comprise a significant fraction of the thermoneutral potential. The first STEP mode, energetically represented next to the room temperature process in the scheme, separates sunlight into thermal and visible radiation. The solar visible generates electronic charge which drives electrolysis charge transfer. The solar thermal component heats the electrolysis and decreases both the E° at this higher T, and the overpotential. The second mode, termed Hy-STEP (on the right) from “hybrid-STEP“, does not separate sunlight, and instead directs all sunlight to heating the electrolysis, generating the highest T and smallest E, while the electrical energy for electrolysis is generated by a separate source (such as by photovoltaic, solar thermal electric, wind turbine, hydro, nuclear or fossil fuel generated electronic charge). As shown on the right side, high relative concentrations of the electrolysis reactant (such as CO_2 or iron oxide will further decrease the electrolysis potential).

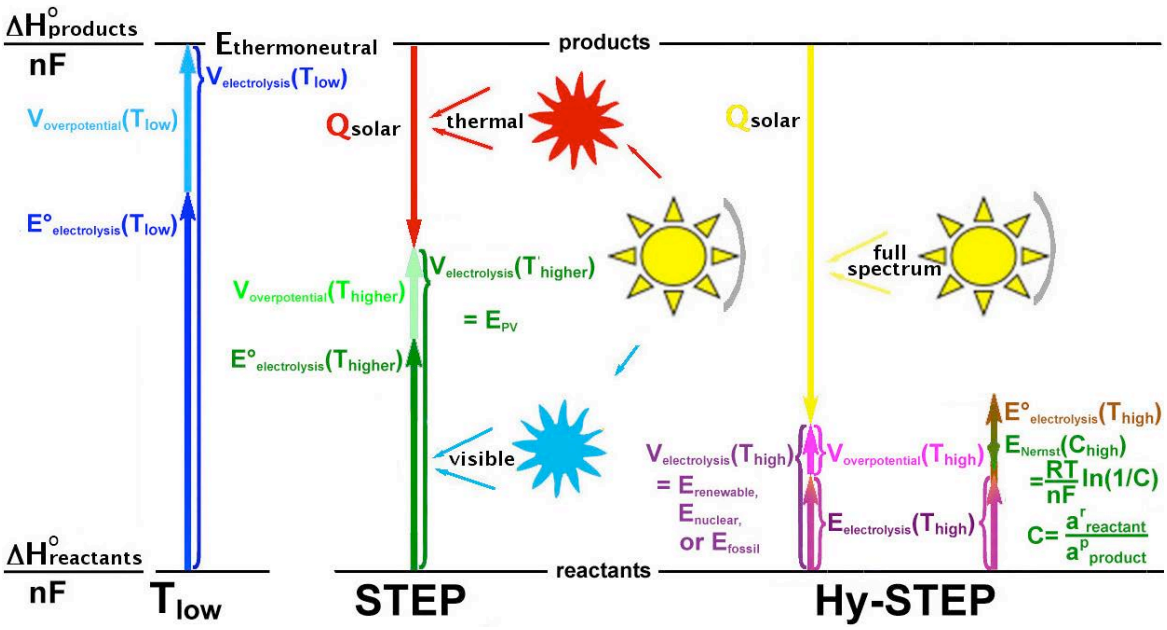

Scheme 4. Comparison of solar energy utilization in STEP and Hy-STEP implementations of the solar thermal electrochemical production of energetic molecules.

Prior investigations of the electrochemistry of carbonates in molten salts tended to focus on reactions of interest to fuel cells,[31] rather than the (reverse) electrolysis reactions of relevance to the STEP reduction of carbon dioxide, typically in alkali carbonate mixtures (Advances in molten carbonate science and technology for fuel cells have been described (K. Sunmacher *Molten Carbonate Fuel Cells*, Wiley-VCH, Weinheim), Germany **2007)**). Such mixtures substantially lower the melting point compared to the pure salts, and would provide the thermodynamic maximum voltage for fuel cells. However, the electrolysis process is maximized in the opposite temperature domain of fuel cells, that is at elevated temperatures which decrease the energy of electrolysis. These conditions provide a new opportunity for effective electrolytic production of staples.

In 2009 we showed that molten carbonate electrolyzers can provide an effective media for solar splitting of CO_2 at high conversion efficiency.[4,59] We find that molten electrolytes present several fundamental advantages compared to solid oxides for CO_2 electrolysis. (i) Molten carbonate electrolyzer provides 10^3 to 10^6 times higher concentration of reactant at the cathode surface than a solid oxide electrolyzer. Solid oxides utilize gas phase reactants, whereas carbonates utilize molten phase reactants. Molten carbonate contains $2x10^{-2}$ mol reducible tetravalent carbon / cm^3. The density of reducible tetravalent carbon sites in the gas phase is considerably lower. Air contains 0.03% CO_2, equivalent to only $1x10^{-8}$ mol of tetravalent carbon / cm^3, and flue gas (typically) contains 10-15% CO_2, equivalent to $2x10^{-5}$ mol reducible C(IV) / cm^3. Carbonate's higher concentration of active, reducible tetravalent carbon sites, logarithmically decreases the electrolysis potential, and can facilitate charge transfer at low electrolysis potentials. (ii) Molten carbonates can directly absorb atmospheric CO_2, whereas solid oxides require an energy consuming pre-concentration process. (iii) Molten carbonates electrolyses are compatible with both solid and gas phase products. (iv) Molten processes have an intrinsic thermal buffer not found in gas phase systems. Sunlight intensity varies over a 24 hour cycle, and more frequently with variations in cloud cover. This disruption to other solar energy conversion processes is not necessary in molten salt processes. The thermal buffer capacity of molten salts has been effective for solar to electric power towers to operate 24/7. These towers concentrate solar thermal energy to heat molten salts, which circulate and via heat exchange boil water to drive conventional mechanical turbines.

The electrolysis of carbon capture in molten carbonates can occur at lower experimental. A constant influx of carbon dioxide to the cell maintains a low concentration of Li_2O. The activity ratio, Θ, of the carbonate reactant to the oxide product in the electrolysis chamber, when high, decreases the cell potentials with the Nernst concentration variation as:

$$E_{CO2/X}(T) = E°_{CO2/X}(T) - 0.0592V \cdot T(K)/(n \cdot 298K) \cdot \log(\Theta);$$
$$n=4 \text{ or } 2, \text{ for } X= C_{solid} \text{ or CO product} \quad (16)$$

For example from eq 16, the expected cell potential at 950°C for the reduction to the CO product is $E_{CO2/CO}$ = 1.17 V -(0.243V /2)·4= 0.68 V, with a high Θ=10,000 carbonate/oxide ratio in the electrolysis chamber.

STEP solar to chemical energy conversion efficiency

The Hy-STEP mode is being studied outdoors with wind or solar CPV generated electricity to drive $E_{electrolysis}$. The STEP mode is experimentally more complex and is presently studied indoors under solar simulator illumination. Determination of the efficiency of Hy-STEP with solar electric is straightforward in the domain in which $E_{electrolysis} < E_{thermoneutral}$ and the coulombic efficiency is high. Solar thermal energy is collected at an efficiency of $\eta_{thermal}$ to decrease the energy from $E_{thermoneutral}$ to $E_{electrolysis}$, and then electrolysis is driven at a solar electric energy efficiency of $\eta_{solar\text{-}electric}$:

$$\eta_{Hy\text{-}STEP\ solar} = (\eta_{thermal} \bullet (E_{thermoneutral}-E_{electrolysis}) + \eta_{solar\text{-}electric} \bullet E_{electrolysis}) / E_{thermoneutral} \quad (17)$$

$\eta_{thermal}$ is higher than $\eta_{solar\text{-}electric}$, and gains in efficiency occur in eq 17 in the limit as $E_{electrolysis}$ approaches 0. $E_{electrolysis}$ = 0 is equivalent to thermochemical, rather than electrolytic, production. As seen in **Fig. 6**, at unit activity $E°_{CO2/CO}$ does not approach 0 until 3000°C. Material constraints inhibit approach to this higher temperature, while electrolysis also provides the advantage of spontaneous product seperation. At lower temperature, small values of $E_{electrolysis}$ can occur at higher reactant and lower product activities, as described in eq 14. In the present configuration sunlight is concentrated at 75% solar to thermal efficiency, heating the electrolysis to 950°C, which decreases the high current density CO_2 splitting potential to 0.9V, and the electrolysis charge is provided by CPV at 37% solar to electric efficiency. The solar to chemical energy conversion efficiency is in accordance with eq 17:

$$\eta_{Hy\text{-}STEP\ solar} = (75\% \bullet (1.46V\text{-}0.90V) + 37\% \bullet 0.90V)/1.46V = 52\% \quad (18)$$

A relatively high concentration of reactants lowers the voltage of electrolysis via the Nernst term in eq 14. With appropriate choice of high temperature electrolyte, this effect can be dramatic, for example both in STEP iron and in comparing the benefits of the molten carbonate to solid oxide (gas phase) reactants for STEP CO_2 electrolytic reduction, sequestration and fuel formation. Fe(III) (as found in the common iron ore, hematite) is nearly insoluble in sodium carbonate, while it is soluble to over 10 m (molal) in lithium carbonate,[8] and a molten carbonate electrolyzer provides 10^3 to 10^6 times higher concentration of reactant at the cathode surface than a solid oxide electrolyzer.

In practice, for STEP iron or carbon capture, we simultaneously drive lithium carbonate electrolysis cells together in series, at the CPV maximum power point (**Fig. 7**). Specifically, a Spectrolab CDO-100-C1MJ concentrator solar cell is used to generate 2.7 V at maximum power point, with solar to electrical energy efficiencies of 37% under 500 suns illumination. As seen in **Fig. 7**, at maximum power, the 0.99 cm^2 cell generates 1.3 A at 100 suns, and when masked to 0.2 cm^2 area generates 1.4 A at 500 suns. Electrolysis electrode surface areas were chosen to match the solar cell generated power. At 950°C at 0.9V, the electrolysis cells generate carbon monoxide at 1.3 to 1.5 A (the electrolysis current stability is shown at the bottom of **Fig. 7**).

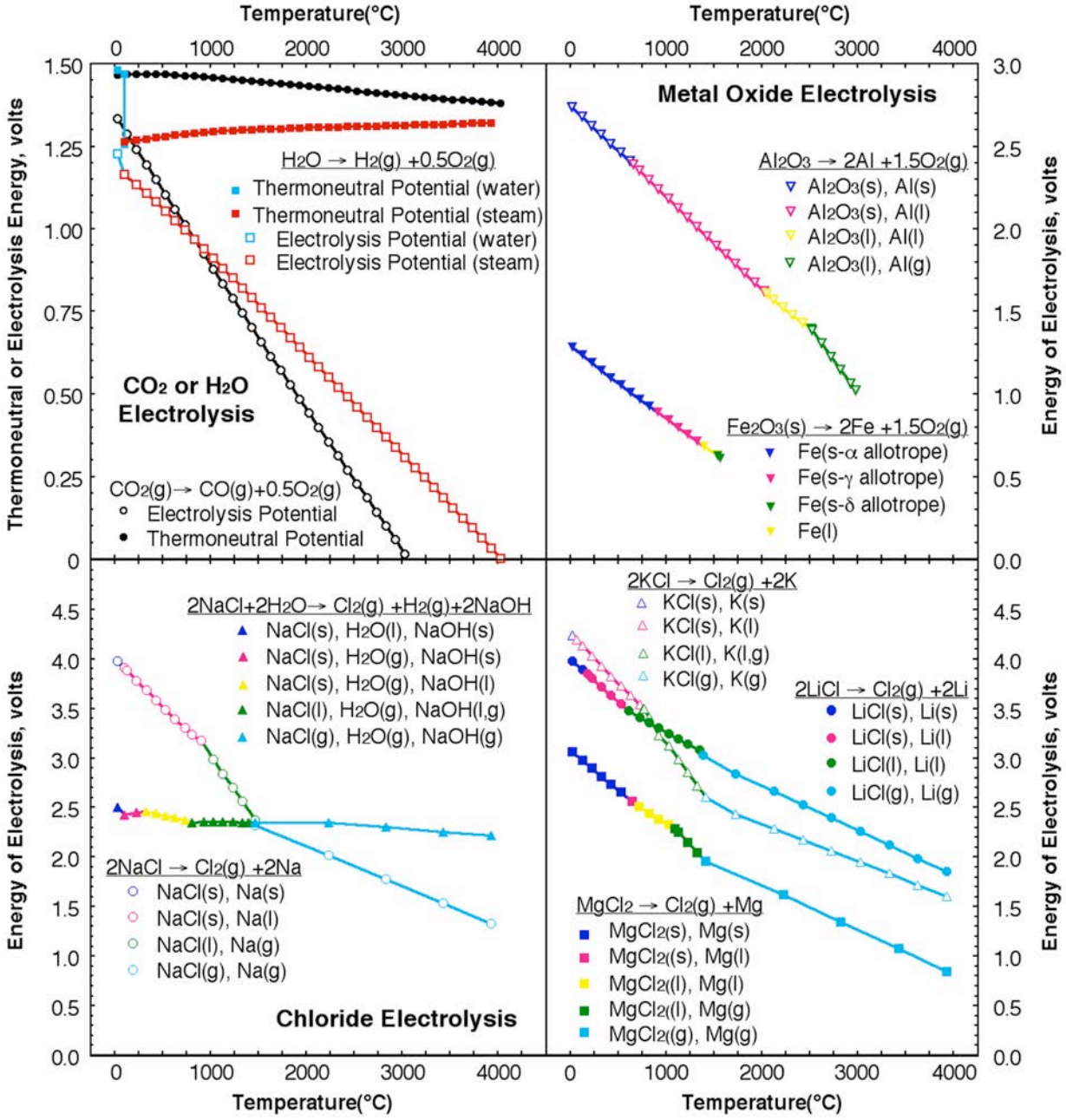

Figure 6. The calculated potential to electrolyze selected oxides (top) and chlorides (bottom). The indicated decrease in electrolysis energy, with increase in temperature, provides energy savings in the **STEP** process in which high temperature is provided by excess solar heat. Energies of electrolysis are calculated from eq 13, with consistent thermochemical values at unit activity using NIST gas and condensed phase Shomate equations.[10] Note with water excluded, the chloride electrolysis decreases (in the lower left of the figure). All other indicated electrolysis potentials, including that of water or carbon dioxide, decrease with increasing temperature. Thermoneutral potentials are calculated with eq 15.

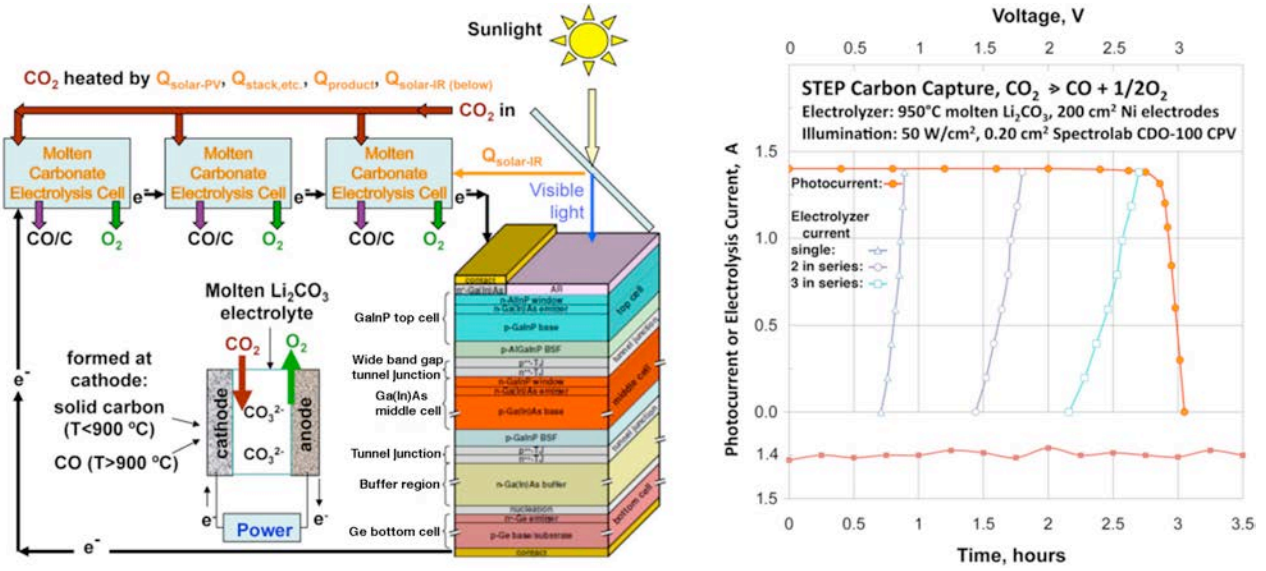

Figure 7. Left: STEP carbon capture in which three molten carbonate electrolysis in series are driven by a concentrator photovoltaic. Sunlight is split into two spectral regions; visible drives the CPV and thermal heats the electrolysis cell. In Hy-STEP (not shown) sunlight is not split and the full spectrum heats the electrolysis cell, and electronic charge is generated separately by solar, wind, or other source. Right: The maximum power point photovoltage of one Spectrolab CPV is sufficient to drive three in series carbon dioxide splitting 950°C molten Li_2CO_3 electrolysis cells. Top: Photocurrent at 500 suns (masked (0.20 cm^2) Spectrolab CDO-100 CPV, or electrolysis current, versus voltage; electrolysis current is shown of one, two or three series 950°C Li_2CO_3 electrolysis cells with 200 cm^2 Ni electrodes. Three in series electrolysis cells provide a power match at the 2.7 V maximum power point of the CPV at 950°C; similarly (not shown), two 750°C Li_2CO_3 electrolysis cells in series provide a power match at 2.7V to the CPV. Bottom: Stable carbon capture (with 200 cm^2 "aged" Ni electrodes at 750°C; fresh electrodes (not shown) exhibit an initial fluctuation as carbon forms at the cathode and Ni oxide layer forms on the anode. The rate of solid carbon deposition gradually increases as the cathode surface area slowly increases in time.

In accord with eq 17 and Scheme 4, Hy-STEP efficiency improves with temperature increase to decrease overpotential and $E_{electrolysis}$, and with increase in the relative reactant activity. Higher solar efficiencies will be expected, both with more effective carbonate electrocatalysts (as morphologies with higher effective surface area and lower overpotential) are developed, and as also as PV efficiencies increase. Increases in solar to electric (both PV, CPV and solar thermal-electric) efficiencies continue to be reported, and will improve eq 18 efficiency. For example, multijunction CPV have been reported improved to $\eta_{PV} = 40.7\%$.[60,61]

Engineering refinements will improve some aspects, and decrease other aspects, of the system efficiency. Preheating the CO_2, by circulating it as a coolant under the CPV (as we currently do in the indoor STEP experiment, but not outdoor, Hy-STEP experiments) will improve the system efficiency. In the present configuration outgoing CO and O_2 gases at the cathode and anode heat the incoming CO_2. Isolation of the electrolysis products will require heat exchangers with accompanying radiative heat losses, and for electrolyses in which there are side reactions or product recombination losses, $\eta_{Hy\text{-}STEP\ solar}$ will decrease proportional to the decrease in coulombic efficiency. At present, wind turbine generated electricity is more cost effective than solar-electric, and we have demonstrated a Hy-STEP process with wind-electric, for CO_2 free production of iron. Addition of long-term (overnight) molten salt insulated storage will permit continuous operation of the STEP process. Both STEP implementations provide a basis for practical, high solar efficiencies.

Components for STEP CO_2 capture and conversion to solid carbon are represented on the left side of **Fig. 7**, and are detailed in references 8. A 2.7 V CPV phootopotential drives three in series electrolyses at 950°C.

Fundamental details of the heat balance are provided in reference 7 and 8. The CPV has an experimental solar efficiency of 37%, and the 63% of insolation not converted to electricity comprises a significant heat source. The challenge is to direct a substantial fraction of this heat to the electrolysis. An example of this challenge is in the first stage of heating, in which higher temperatures increases CO_2 preheat, but diminishes the CPV power. Heating of the reactant CO_2 is a three tier process in the current configuration: the preheating of room temperature CO_2 consists of either (1a) flow-through a heat exchange fixed to the back of the concentrator solar cell and/or (1b) preheating to simulate CO_2 extracted from an available heat source such as a hot smoke (flue) stack, (2) secondary heating consists of passing this CO_2 through a heat exchange with the outgoing products, (3) tertiary heat is applied through concentrated, split solar thermal energy (**Fig. 7**).

An upper limit to the energy required to maintain a constant system temperature is given in the case in which neither solar IR, excess solar visible, nor heat exchange from the environment or products would be applied to the system. When an 0.90V electrolysis occurs, an additional 0.56 V, over E_{tn} =1.46V , is required to maintain a constant system temperature. Hence, in the case of three electrolyses in series, as in **Fig. 7**, an additional 3x0.56V=1.68V will maintain constant temperature. This is less than the 63% of the solar energy (equivalent to 4.6V) not used in generating the 2.7 V of maximum power point voltage of electronic charge from the CPV in this experiment. Heating requirements are even less, when the reactant activity is maintained at a level that is higher than the product activity. For example, this is accomplished when products are continuously removed to ensure that the partial pressure of the products is lower than that of the CO_2. This lowers the total heat required for temperature neutrality to below that of the unit activity thermoneutral potential 1.46V.

The STEP effective solar energy conversion efficiency, η_{STEP}, is constrained by both photovoltaic and thermal boost conversion efficiencies, η_{PV} and $\eta_{thermal\text{-}boost}$.[62] Here, the CPV sustains a conversion efficiency of η_{PV} = 37.0%. In the system, passage of electrolysis current requires an additional, combined (ohmic, & anodic + cathodic over-) potential above the thermodynamic potential. However, mobility and kinetics improve at higher temperature to decrease this overpotential. The generated CO contains an increase in oxidation potential compared to carbon dioxide at room temperature ($E_{CO2/CO}$(25°C)= 1.33 V for $CO_2 \rightarrow CO + 1/2O_2$ in **Fig. 6**), an increase of 0.43 V compared to the 0.90 V used to generate the CO. The electrolysis efficiency compares the stored potential to the applied potential, $\eta_{thermal\text{-}boost} = E°_{electrolysis}(25°C) / V_{electrolysis}(T)$. [8] Given a stable temperature electrolysis environment, the experimental STEP solar to CO carbon capture and conversion efficiency is the product of this relative gain in energy and the electronic solar efficiency:

$$\eta_{STEP} = \eta_{PV} \cdot \eta_{thermal\text{-}boost} = 37.0\% \cdot (1.33V/0.90V) = 54.7\% \quad (19)$$

Ohmic and overpotential losses are already included in the measured electrolysis potential. This 54.7% STEP solar conversion efficiency is an upper limit of the present experiment, and as with the Hy-STEP mode, improvements are expected in electrocatalysis and CPV efficiency. Additional losses will occur when beam splitter and secondary concentrator optics losses, and thermal systems matching are incorporated, but serves to demonstrate the synergy of this solar/photo/electrochemical/thermal process, leads to energy efficiency higher than that for solar generated electricity,[60,61] or for photochemical,[63] photoelectrochemical,[64,65] solar thermal,[66] or other CO_2 reduction processes.[67]

The CPV does not need, nor function with, sunlight of energy less than that of the 0.67 eV bandgap of the multi-junction Ge bottom layer. From our previous calculations, this thermal energy comprises 10% of AM1.5 insolation, which will be further diminished by the solar thermal absorption efficiency and heat exchange to the electrolysis efficiency,[54] and under 0.5 MW m^{-2} of incident sunlight (500 suns illumination), yields ~50 kW m^{-2}, which may be split off as thermal energy towards heating the electrolysis cell without decreasing the CPV electronic power. The CPV, while efficient, utilizes less than half of the super-bandgap ($h\nu$ > 0.67 eV) sunlight. A portion of this > ~250 kW m^{-2} available energy, is extracted through heat exchange at the backside of the CPV. Another useful source for consideration as supplemental heat is industrial exhaust. The temperature of industrial flue stacks varies widely, with fossil fuel source and application, and ranges up to 650°C for an open circuit gas turbine. The efficiency of thermal energy transfer will limit use of this available heat.

A lower limit to the STEP efficiency is determined when no heat is recovered, either from the CPV or remaining solar IR, and when heat is not recovered via heat exchange from the electrolysis products, and when an external heat source is used to maintain a constant electrolysis temperature. In this case, the difference between the electrolysis potential and the thermoneutral potential represents the enthalpy required to keep the system from cooling. In this case, our 0.9V electrolysis occurs at an efficiency of (0.90V/1.46V) · 54.7% = 34%. While the detailed STEP energy analysis, for example for CO_2 to CO splitting, is more complex than that of the Hy-STEP mode, more solar thermal energy is available including a PV's unused or waste heat to drive the process and to improve the solar to chemical energy conversion efficiency. We determine the STEP solar efficiency over the range from inclusion of no solar thermal heat (based on the enthalpy, rather than free energy, of reaction) to the case where the solar thermal heat is sufficient to sustain the reaction (based on the free energy of reaction). This determines the efficiency range, as chemical flow out to the solar flow in (as measured by the increase in chemical energy of the products compared to the reactants), from 34% to over 50%.

References

12. E. Worrell, L. Price, N. Martin. *Ann. Rev. Energy Environ.* 2001, **26**, 303.
13. T. West, A. McBride. *Agr. Ecosys. Environ.* 2005, **108**, 145.
14. NIST-CHEMWeb Thermochemical Data., *J. Phys. Chem. Ref. Data*, 1998; data interactively available at: http://webbook.nist.gov/chemistry/form-ser.html.
15. Glenn Research Center NASA, *ThermoBuild access to NASA Glenn thermodynamic CEA database*, 2006; data available at: http://www.grc.nasa.gov/WWW/CEAWeb/ceaThermoBuild.htm
16. T. Oates, Lime and Limestone, *Kirk-Othmer Enc Chem Tech.*, 1-53, Wiley online library, 2010 as DOI: 10.1002/0471238961.1209130507212019.a01.pub3.
17. K. Tanimoto, *et al.* Cell performance of molten-carbonate fuel-cell with alkali and alkaline-earth carbonate mixtures. *J. Pow. Sources* 1992, **39**, 285-297.
18. M. Cassir, M. Olivery, V. Albin, B. Malinowska & J. Devynck, J. Thermodynamic and electrochemical behavior of nickel in molten Li_2CO_3-Na_2CO_3 modified by addition of calcium carbonate. *J. Electroanal. Chem*. 1998, **452**, 127-137.
19. M. Roli, *Bull. Soc. Chim. Fr.*, 1964, 2104.
20. A. Navrotsky, R. Putnam, C. Winbo, & E. Rosen, Thermochemistry of double carbonates in the K_2CO_3-$CaCO_3$ system. *Amer. Mineralogist*, 1997, **82**, 546-8.
21. C. Winbo, E. Rosen & M. Heim, Thermal analytical study of the decomposition of $K_2Ca_2(CaO_3)_3$. *Acta Chemica Scand.* 1998, **52**, 431-4.
22. A. Cooper, J. Gittins & O. Tuttle, System Na_2CO_3-K_2CO_3-$CaCO_3$ at 1 kilobar and its significance in carbonatite petrogenesis. *Amer. J. Sci.*, 1975, 534-560.
23. S. Frangini & S. Scaccia, Sensitive Determination of Oxygen Solubility in Alkali Carbonate Melts. *J. Electrochem. Soc*, 2004, **151**, A1251-A1256.
24. JADE, 6.1; Materials Data, Inc: Livermore, CA, 2002.
25. S. Licht, *et al.* Analysis of Ferrate(VI) compounds and Super-Iron Fe(VI) Battery Cathodes. FTIR, XRD, UV/Vis, ICP, Electrochemical and Chemical, Characterization. *J Power Sources,* 2001**, 101**, 167-176.
26. N. Mahasenan, S. Smith & K. Humphreys, "The Cement Industry and Global Climate Change: Current and Potential Future Cement Industry CO_2 Emissions". *Greenhouse Gas Control Technologies – 6th International Conference*. Oxford: Pergamon. 2003, pp. 995–1000. ISBN 9780080442761. Retrieved 2008-04-09.
27. Iron and steel, IEA ETASP Tech Brief, 102, May 2010, at: http://www.iea-etsap.org/web/E-TechDS/PDF/I02-Iron&Steel-GS-AD-gct.pdf
28. T. West & A. McBride, The contribution of agricultural lime to carbon dioxide emissions in the United States: dissolution, transport, and net emissions. *Agr. Ecosys. Environ,* 2005, **108**, 145-154.
29. C. George, Carbon Monoxide. *Kirk-Othmer Enc Chem Tech.*, 2001, **5**, 1, Wiley online library (2001) as DOI: 10.1002/0471238961.0301180216090518.a02.pub2
30. E. Barbier, E. How is the global green deal going?. *Nature,* 2010. *464.* 832.
31. K. Sunmacher, K. *Molten Carbonate Fuel Cells*, 2007. Weinheim: Wiley-VCH.
32. BrightSource. 2012. at: http://brightsourceenergy.com
33. AREVA. 2012. at: http://www.areva.com/EN/solar-220/areva-solar.html
34. Siemens. 2011. at: http://www.siemens.com/press/pool/de/pressemitteilungen/2011/renewable_energy/ERE201102037e.pdf
35. SolarReserve. 2012. at: http://www.solarreserve.com/
36. Amonix. 2012. at: http://www. amonix.com/
37. Energy Innovations. 2012. at: http://www.energyinnovations.com/
38. R. Pitz -Paal, 2007. High Temperature Solar Concentrators. *Solar Energy Conversion and*

Photoenergy Systems, Eds. Galvez, J. B.; Rodriguez, S. M. Oxford: *EOLSS* Publishers.
39. Gemasolar, Torreso Energy, Gemasolar CSP at: http://www.torresolenergy.com/TORRESOL/Press/gemasolar-wil-be-the-main-project-presented-by-torresol-energy-in-solar-power-internacional-2011
40. Brightsource and SolarReserve at CSO at: http://www.greentechmedia.com/articles/read/brightsource-energy-files-for-250m-ipo-an-analysis/
41. B. Prior, Cost and LCOE by Generation Technology, 2009-2020, GTM research, Nov. 2011, at: http://www.greentechmedia.com/images/wysiwyg/research-blogs/GTM-LCOE-Analysis.pdf
42. W. Tahil, "The Trouble with Lithium 2; Under the Microscope", 2008, 54 pages, Meridan International Research, Martainsville, France.
43. A. Fujishima, K. Honda, *Nature*, 1972, **238**, 37.
44. Z. Zou, Y. Ye, K. Sayama, H. Arakawa, *Nature*, 2001, **414**, 625.
45. S. Licht, B. Wang, S. Mukerji, T. Soga, M. Umento, H. Tributsh, *J. Phys. Chem. B*, 2000, **104**, 8920.
46. S. Licht, *J. Phys. Chem. B*, **2001**, *105*, 6281.
47. S. Licht, L. Halperin, M. Kalina, M. Zidman, N. Halperin, *Chem. Comm*. 2003, **2003**, 3006.
48. S. Licht, *Chem. Comm*. 2005, **2005**, 4623.
49. S. Licht, *Electrochem. Comm*. 2002, **4**, 789.
50. A. J. deBethune, T. S. Licht, *J. Electrochem. Soc*., 1959, **106**, 616.
51. M. W. Chase; b) *J. Phys. Chem. Ref. Data*, 1998, **9**, 1.
52. J. O'M. Bockris, *Energy Options,* Halsted Press, NY, 1980.
53. S. Licht, *Electrochem. Comm*. 2002, 4, 789.
54. S. Licht, *J. Phys. Chem. B*, 2003, **107**, 4253.
55. T. S. Light, S. Licht, A. C. Bevilacqua, *Electrochem & Sol State Lett.*, 2005, **8**, E16.
56. T. S. Light, S. Licht, *Anal. Chem.*, 1987, **59**, 2327.
57. S. Licht, *Anal. Chem.*, 1985, **57**, 514.
58. S. Licht, K. Longo, D. Peramunage, F. Forouzan, *J. Electroanal. Chem.*, 1991, **318**, 119.
59. S. Licht. B. Wang, S. Ghosh, H. Ayub, D. Jiang, J. Ganely, *J. Phys. Chem. Lett.* **2010**, *1*, 2363.
60. R.R. King, D. C. Law, K. M. Edmonson, C. M. Fetzer, G. S. Kinsey, H. Yoon, R. A. Sherif, N. H. Karam, *Appl. Phys. Lett.* **2007**, *90*, 183516.
61. M. Green, K. Emery, Y. Hishikawa, W. Warata, *Prog. Photovoltaics*, **2011**, *19*, 84.
62. S. Licht, B. Wang, H. Wu, *J. Phys. Chem., C* **2011**, *115*, 11803.
63. J. E. Miller, J. E.; Allendorf, M. D.; Diver, R. B.; Evans, L. R.; Siegel, N. P.; Stuecker, J. N. *J. Mat. Sci.* **2008**, *43*, 4714.
64. *Semiconductor Electrodes and Photoelectrochemistry*, (Ed: S. Licht), Wiley-VCH, Weinheim, Germany **2002**.
65. E. E. Barton, D. M. Rampulla, and A. B. Bocarsly, *J. Am. Chem. Soc.,* **2008**, *130*, 6342.
66. Y. Woolerton, Y., W.; Sheard, S.; Reisner, E.; Pierce, E.; Ragsdale, S. W.; Armstrong, F. A. *J. Amer. Chem. Soc.* **2010**, *132*, 2132.
67. E. Benson, C. P. Kubiak, A. J, Sathrum, J. M. N. Smieja *Chem. Soc. Rev.* **2009**, *38*, 89.
68.